Rock and Soil Mechanics

Volume 42 | Issue 11 Article 8

2-23-2022

Dynamic responses of saturated soft soil foundation under high-speed train load

Jing HU

Yue TANG

Jia-kang ZHANG

Tao DENG

Custom Citation

HU Jing, TANG Yue, ZHANG Jia-kang, DENG Tao. Dynamic responses of saturated soft soil foundation under high-speed train load[J]. Rock and Soil Mechanics, 2021, 42(11): 3169-3181.

Rock and Soil Mechanics 2021 42(11): 3169−3181 ISSN 1000−7598
https: //doi.org/10.16285/j.rsm.2021.5572 rocksoilmech.researchcommons.org/journal

Dynamic responses of saturated soft soil foundation under high-speed train load

HU Jing, TANG Yue, ZHANG Jia-kang, DENG Tao
College of Civil Engineering, Fuzhou University, Fuzhou, Fujian 350108, China

Abstract: Based on Biot's theory of porous media, this paper proposes a coupled vehicle-track-saturated foundation model to study the dynamic responses of saturated soft soil foundation under high-speed train load via two-and-half dimensional finite element method (2.5D FEM). It is found that the ratio of train speed c and soil Darcy permeability k_{D} (c/k_{D}) determines the extent to which maximum excess pore pressures build up in saturated soft soil under the train load when the load speed is lower than the critical speed. For a saturated soil of a particular stiffness, if c/k_{D} is less than or equal to 3×10^4, the soil can be regarded as highly permeable relating to the load velocity. In this case, almost no excess pore pressure is developed, and the saturated soil can be modeled using a single-phase medium. There is a critical value of c/k_{D} for the development of excess pore pressure, corresponding to which the maximum excess pore pressure increases with increasing c/k_{D}. Above this critical value of c/k_{D}, the maximum excess pore pressure remains independent of c/k_{D}. The amplitude and influencing zone of effective stress are mainly controlled by the train speed and soil permeability for saturated soft soil foundation. The response of displacement is mainly controlled by the train speed. Significant Mach effects have been induced in the saturated soil foundation by the moving train when the train speed reaches or exceeds the critical velocity of the track-foundation system.

Keywords: saturated soft soil foundation; high-speed train; 2.5D FEM; excess pore pressure; critical velocity

1 Introduction

High-speed train loads are characterized by short duration, high frequency, and periodicity. For saturated soft ground with low permeability, the high-speed train loads can cause excess pore pressure in the ground and may not be completely dissipated before the next train arrives, resulting in the accumulation of excess pore pressure. The generation and accumulation of excess pore pressure will reduce the effective stress in the saturated soil and increase the ratio of shear force to effective stress, probably causing significant soil strain and displacement, and even worse, affecting traffic safety. A large amount of saturated soft soil exists along the southeast coast of China. Thus, with the density of the high-speed railway network in coastal areas increasing and the speed of trains rising, studying the dynamic response of saturated soft ground under the high-speed train loads is crucial to ensure traffic safety.

To study the dynamic response of saturated soil under load, Biot[1–2] established a wave propagation theory and control equations for saturated porous media based on the theory of elastic wave propagation, considering the coupled motion of elastic soil skeleton and pore fluid. Zienkiewicz and Shiomi[3], Siddharthan et al.[4], and others derived semi-analytic solutions in two-dimensional space based on Biot's equations. Lu et al.[5–6] solved the semi-analytic solution in the 3D saturated half-space body under moving point loads, which became a benchmark for verifying the accuracy of the numerical model. In recent years, the 2.5-dimensional finite element method (2.5D FEM) has also been applied to solve the dynamic response of saturated two-phase media under moving loads to improve the computational efficiency of the 3D FEM model[7–14]. It has been shown that the response of saturated two-phase media differs from that of single-phase elastic media under moving loads. Under low-speed loading, the vertical displacement of saturated two-phase media is smaller than that of single-phase elastic media. However, under high-speed loading, saturated two-phase media have larger vertical displacement[7] and smaller stress response compared to single-phase elastic media[15]. Cai et al.[16–17] found in their study of the dynamic response in saturated foundations under train loading that the larger the train speed, the higher the excess pore pressure in the saturated foundation. Theodorakopoulos et al.[18–19] found that porosity and permeability significantly affected the excess pore pressure response in saturated soft soil. Li et al.[20] analyzed the effect of trains' high speed on the ground vibration of saturated roadbeds. Qian et al.[21] carried out a theoretical study on the dynamic response of saturated foundations under high-speed moving loads and found that the amplification effect of dynamic stress increased with the depth of the foundation. With the application of Biot theory to the study of the dynamic response of saturated soils around tunnels, Yuan et al.[22–23] studied the dynamic response of saturated soil around tunnels induced by moving loads through a 2D model, and a subsequent study found that the excess pore pressure increased with decreasing soil permeability and increasing load velocity. Di et al.[24–25] studied the spatial distribution of stresses and excess pore pressure in saturated soil around tunnels. He et al.[26] established a coupled FEM-BEM model to study the dynamic

Received: 13 May 2021 Revised: 20 July 2021
This work was supported by the Natural Science Foundation of Fujian Province (2020J05107), the Open Research Fund of the Ministry of Education Key Laboratory of Soft Soils and Geoenviromental Engineering (Zhejiang University) (2020P05) and the Start-up Fund of Fuzhou University (0050-510086 GXRC-20024).
First author: HU Jing, female, born in 1991, PhD, Assistant research fellow, mainly engaged in research on dynamic response of railway subgrade and dynamic problems of subway tunnel. E-mail: jingh@fzu.edu.cn

response of saturated soil around a special tunnel. Considering the anisotropy and stratification of natural soil, studies on the dynamic response of transverse isotropic saturated foundations[27–31] and stratified saturated soil[32–33] have also appeared in recent years.

The above studies focused on the important effects of load movement velocity and soil permeability coefficient on the dynamic response, such as excess pore pressure. However, by far, the research on the dynamic response of the foundation under high-speed train loads, especially when the train speed approaches or even exceeds the critical velocity, has been mainly based on the single-phase elastic foundation model[34–41], and there are few studies on the basis of saturated foundation model.

Therefore, a 2.5D FEM model of the coupled vehicle-track-saturated foundation system based on the Biot wave theory of porous media is established in this study to investigate the dynamic response of the saturated soft ground foundation under high-speed train loads. The dynamic response of the saturated soft foundation under train loads is analyzed when the train speed is less than, equal to, and more than the critical velocity, respectively. And the effect of the ratio of train speed to the permeability coefficient (c / k_{D}) of the saturated soft soil on the excess pore pressure, effective stress, and displacement response is evaluated in the present study.

2 Solution of dynamic governing equations for saturated porous media

2.1 Basic theory of saturated porous media

Biot dynamic control equations for homogeneous saturated porous media are[42]

(1) Equilibrium equation

$$\sigma_{ij,j} = \rho_{\mathrm{b}}\ddot{u}_i + \rho_{\mathrm{f}}\ddot{w}_i \tag{1}$$

(2) Seepage equation

$$p_i = -b\dot{w}_i - \rho_{\mathrm{f}}\ddot{u}_i - m\ddot{w}_i \tag{2}$$

(3) Continuity equation

$$\dot{p} = -\alpha M\dot{u}_{i,i} - M\dot{w}_{i,i} \tag{3}$$

(4) Constitutive equation

$$\sigma_{ij} = \mu(u_{i,j} + u_{j,i}) + \lambda\delta_{ij}\theta - \alpha\delta_{ij}p \tag{4}$$

where σ_{ij} and p are the stress on the soil skeleton and the pore pressure in the soil unit, respectively; u_i and ω_i are the displacement of the soil skeleton and the average displacement of the pore fluid relative to the soil skeleton, respectively; the density of the saturated soil is $\rho_{\mathrm{b}} = n\rho_{\mathrm{f}} + (1-n)p_{\mathrm{s}}$, and ρ_{f} and ρ_{s} are the densities of the pore fluid and soil particles, respectively, and n is the porosity; m is the effective density, $m = a_\infty\rho_{\mathrm{f}}/n$, where $a_\infty = 1/\sqrt{n}$ is a parameter to measure the pore curvature of the soil; $b = \rho_{\mathrm{f}}g/k_{\mathrm{D}}$ represents the viscous coupling effect between the pore fluid and the soil particles, where k_D is the Darcy permeability coefficient of saturated soil (m/s), g is the acceleration of gravity; α ($\alpha = 1 - \frac{K}{K_{\mathrm{s}}}$) and M ($M = \frac{n}{K_{\mathrm{f}}} + \frac{\alpha - n}{K_{\mathrm{s}}}$) are the Biot constants, and K, K_s and K_f are the bulk modulus of the soil skeleton, soil particles, and pore fluid, respectively; subscripts i, j=x, y, z are tensor signs and follow the summation convention; λ and μ are the Lame constants of the soil skeleton, respectively; superscripts '.' and '..' denote the first-order and second-order derivatives with respect to time, repectively; and δ_{ij} is Kronecker delta function.

After integrating Eq.(3) over time t and substituting the equation and Eq. (4) into Eqs. (1) and (2), the complete Biot dynamic control equation can be obtained as

$$\mu u_{i,jj} + (\lambda + \alpha^2 M + \mu)u_{j,ji} + \alpha M w_{j,ji} = \rho_{\mathrm{b}}\ddot{u}_i + \rho_{\mathrm{f}}\ddot{w}_i \tag{5}$$

$$\alpha M u_{j,ji} + M w_{j,ji} = \rho_{\mathrm{f}}\ddot{u}_i + m\ddot{w}_i + b\dot{w}_i \tag{6}$$

2.2 2.5D finite element solution

Define the Fourier transform on time and space,

$$\tilde{\bar{u}}(\xi_x, y, z, \omega) = \int_{-\infty}^{+\infty}\int_{-\infty}^{+\infty} u(x, y, z, t)\mathrm{e}^{\mathrm{i}\xi_x x}\mathrm{e}^{-\mathrm{i}\omega t}\mathrm{d}x\mathrm{d}t \tag{7}$$

where x represents the direction along the orbit; t is the time; ζ_x is the wavenumbers along the x-direction; ω is the angular frequency. The superscripts '-' and '~' are the quantities in the frequency and wavenumber (f-k) domains, respectively.

The corresponding Fourier inverse transform is

$$u(x, y, z, t) = \frac{1}{4\pi^2}\int_{-\infty}^{+\infty}\int_{-\infty}^{+\infty} \tilde{\bar{u}}(\xi_x, y, z, \omega)\mathrm{e}^{\mathrm{i}\xi_x x}\mathrm{e}^{\mathrm{i}\omega t}\mathrm{d}\xi_x\mathrm{d}\omega \tag{8}$$

Substituting Eq.(7) into Eqs.(5) and (6), the expression of Biot's dynamical equation in the f–k domain is obtained:

$$\begin{aligned}&\mu\tilde{\bar{u}}_{i,jj} + (\lambda + \mu)\tilde{\bar{u}}_{j,ji} + \alpha^2 M\tilde{\bar{u}}_{j,ji} + \alpha M\tilde{\bar{w}}_{j,ji} + \\ &\rho_{\mathrm{b}}\omega^2\tilde{\bar{u}}_i + \rho_{\mathrm{f}}\omega^2\tilde{\bar{w}}_i = 0\end{aligned} \tag{9}$$

$$\alpha M\tilde{\bar{u}}_{j,ji} + M\tilde{\bar{w}}_{j,ji} + \rho_{\mathrm{f}}\omega^2\tilde{\bar{u}}_i + m\omega^2\tilde{\bar{w}}_i - \mathrm{i}\omega\frac{\rho_{\mathrm{f}}g}{k_{\mathrm{D}}}\tilde{\bar{w}}_i = 0 \tag{10}$$

Yuan[22–23], Gao et al.[7], and Bian et al.[43] have derived the solution process of the equations in the f–k domain, which will not be detailed here. The final matrix equation obtained for the 2.5D FEM solution is,

$$(\boldsymbol{K}_1 + \boldsymbol{K}_2 - \boldsymbol{M}_1)\tilde{\bar{\boldsymbol{U}}} - (\boldsymbol{L}_1 - \boldsymbol{M}_2)\tilde{\bar{\boldsymbol{W}}} = \tilde{\bar{\boldsymbol{F}}}^{\mathrm{s}} \tag{11}$$

$$(\boldsymbol{K}_3 - \boldsymbol{M}_3)\tilde{\bar{\boldsymbol{U}}} - (\boldsymbol{L}_2 - \boldsymbol{M}_4)\tilde{\bar{\boldsymbol{W}}} = \tilde{\bar{\boldsymbol{F}}}^{\mathrm{f}} \tag{12}$$

where $\boldsymbol{M}$ is the mass matrix; $\boldsymbol{K}$ and $\boldsymbol{L}$ are the stiffness matrices; $\boldsymbol{U}$ and $\boldsymbol{W}$ are the displacement matrix of soil skeleton and the relative displacement matrix of pore fluid, respectively; and $\boldsymbol{F}^{\mathrm{s}}$ and $\boldsymbol{F}^{\mathrm{f}}$ are the external load vectors. The expressions of each matrix are shown in appendix A.

https://rocksoilmech.researchcommons.org/journal/vol42/iss11/8
DOI: 10.16285/j.rsm.2021.5572

2.3 Coupled vehicle-track-subgrade system

The track is simplified as an Euler beam laid on the subgrade. According to the Euler beam dynamic equation, the vibration of the track when the wheel load p_{M} is applied can be described as

$$EI_{\mathrm{r}}\frac{\partial^4 u_{\mathrm{r}}}{\partial x^4}+m_{\mathrm{r}}\frac{\partial^2 u_{\mathrm{r}}}{\partial t^2}=f_{\mathrm{IT}}(x,t)+p_{\mathrm{M}}(x,t) \tag{13}$$

where u_{r} is the deformation of the track; E_{Ir} is the bending stiffness of the rail; m_{r} is the mass of the track; and f_{IT} and p_{M} are the reaction force of the contact point of the subgrade and the force of the whole vehicle load applied on the surface of the rail, respectively. The Fourier transform pair is defined by Eqs. (7) and (8) can be obtained:

$$(EI_{\mathrm{r}}\xi_x^4+m_{\mathrm{r}}\omega^2)\tilde{\bar{u}}_{\mathrm{r}}=\bar{f}_{\mathrm{IT}}(\xi_x,\omega)+\tilde{\bar{p}}_{\mathrm{M}}(\xi_x,\omega) \tag{14}$$

Expressed as a matrix,

$$(\boldsymbol{K}_{\mathrm{T}}+\boldsymbol{\omega}^2\boldsymbol{M}_{\mathrm{T}})\tilde{\bar{\boldsymbol{U}}}_{\mathrm{T}}=-\tilde{\bar{\boldsymbol{F}}}_{\mathrm{IT}}+\tilde{\bar{\boldsymbol{P}}}_{\mathrm{M}} \tag{15}$$

where $\boldsymbol{U}_{\mathrm{T}}$ is the 3D displacement response of the track nodes, containing the vertical displacement u_{r} and two horizontal displacements of the track; $\boldsymbol{K}_{\mathrm{T}}$, $\boldsymbol{M}_{\mathrm{T}}$, and $-\boldsymbol{F}_{\mathrm{IT}}$ are the stiffness matrix of the track, mass matrix of the track, and the reaction force vector of subgrade surface, respectively; $\boldsymbol{P}_{\mathrm{M}}$ is the force vector of the whole train load applied on the rail surface, according to the quarter vehicle body model theory[44], and its expression is $p_{\mathrm{M}}(x,t)=\sum_{k=1}^{M}\sum_{h=1}^{4}p_{kh}(x-ct)$ (k is the carriage number and h is the h-th set of wheel pair). The wheel–rail force of the front and rear bogies of the k-th carriage is expressed as

$$\begin{aligned}&\sum_{i=1}^{4}p_{kh}(x-ct)=p_{k1}\delta(x-ct+\textstyle\sum_{h=0}^{k-1}L_h+x_0)+\\&p_{k2}\delta(x-ct+a_k+\textstyle\sum_{h=0}^{k-1}L_h+x_0)+\\&p_{k3}\delta(x-ct+a_k+b_k+\textstyle\sum_{h=0}^{k-1}L_h+x_0)+\\&p_{k4}\delta(x-ct+2a_k+b_k+\textstyle\sum_{h=0}^{k-1}L_h+x_0)\end{aligned} \tag{16}$$

where p_{k1}, p_{k2}, p_{k3}, and p_{k4} are the axle weights of each wheel pair of the carriage k respectively; L_k is the length of the k-th carriage; x_0 is the distance from the observation point to the 1st wheel pair; a_k is the length of the bogie; b_k is the distance between the center of two bogies; c is the speed of the train.

According to the displacement consistency and force equilibrium condition of the interaction points on the contact surface of the track and the subgrade, the finite element expressions of the integrated track and the subgrade are obtained by eliminating $\boldsymbol{F}^{\mathrm{s}}$, and the dynamic equations of the whole coupled vehicle–track–subgrade system are as follows:

$$\begin{bmatrix}\boldsymbol{K}_1+\boldsymbol{K}_2+\boldsymbol{K}_{\mathrm{T}}-\omega^2(\boldsymbol{M}_1+\boldsymbol{M}_{\mathrm{T}}) & \boldsymbol{L}_1-\omega^2\boldsymbol{M}_2\\ \boldsymbol{K}_3-\omega^2\boldsymbol{M}_3 & \boldsymbol{L}_2-\omega^2\boldsymbol{M}_4\end{bmatrix}\begin{bmatrix}\tilde{\bar{\boldsymbol{U}}}\\ \tilde{\bar{\boldsymbol{W}}}\end{bmatrix}=\begin{bmatrix}\tilde{\bar{\boldsymbol{P}}}_{\mathrm{M}}\\ \tilde{\bar{\boldsymbol{F}}}^{\mathrm{f}}\end{bmatrix} \tag{17}$$

Bian et al.[43] used the multilayer damping boundary approach[45] in solving the dynamic response of a saturated foundation, which simulated the dynamic response of a saturated semi-infinite space well. Therefore, this paper uses the multilayer damping boundary to absorb the wave at the model boundary.

2.4 Model validation

Lu et al.[6] used a semi-analytic approach to obtain a semi-analytic solution for a 3D saturated half- space (Fig. 1) under moving point loads, which became a benchmark for validating subsequent numerical methods. In this section, based on the foundation soil parameters provided in Lu et al.[6] (Table 1), a saturated half-space model is developed using the 2.5D FEM, and the computational results in this study are verified against the semi-analytical solution proposed by Lu et al.[6].

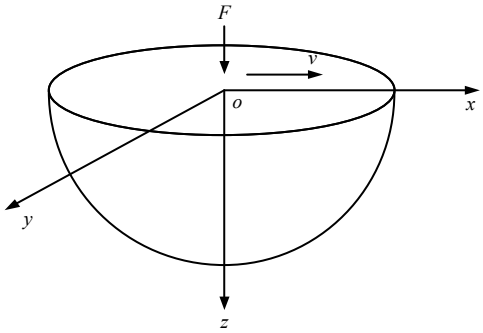

Fig. 1 Half-space saturated medium subjected to a moving point load[6]

Table 1 Parameters used for saturated soil[6]

Biot constant α	Biot constant M /MPa	Elastic modulus E /MPa	Shear modulus G /MPa	Poisson's ratio ν	Soil grain density ρ_{s} /(kg • m^{-3})	Fluid density ρ_{f} /(kg • m^{-3})	Porosity n	Permeability coefficient k_{D} /(m • s^{-1})	Effective density m /(kg • m^{-3})
0.95	5 000	6 744.6	2 997.6	0.125	2 500	1 000	0.3	1×10^{-6}	6 670

The displacement and excess pore pressure response of the observation point (x, 1, 1) when the unit load moves at a unit load of 121 m/s are given in Fig. 2. In the figure, the displacement is normalized by multiplying by Ga_{R}^2/F, where F=1 N, a_{R}=1.0 m. And the excess pore pressure is multiplied by a_{R}^2/F, where F is the unit load, and a_{R} is the reference length. From Fig. 2, it can be found that the displacement response u_z and the excess pore pressure response p obtained from the 2.5D FEM calculation agree with the semi-analytical solution.

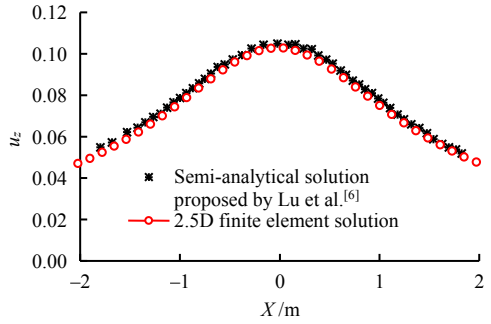

(a) Vertical displacement

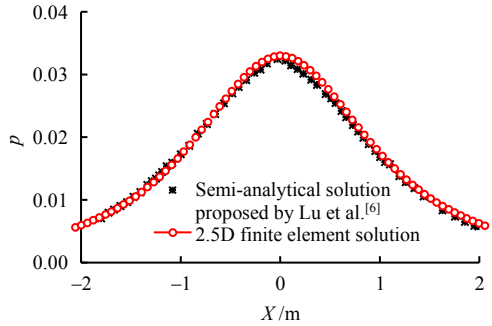

(b) Excess pore pressure

Fig. 2 Verification of 2.5D FEM for saturated medium

3 Numerical analysis

3.1 Overview of numerical simulation

3.1.1 Model introduction

In this section, a 2.5D FEM model of the coupled track–subgrade–saturated foundation system is established, as shown in Fig. 3. The width of the model is 100 m, and the depth is 50 m. The size of the core area is 40 m × 30 m, and the maximum grid size in the core area is 0.5 m × 0.5 m; the maximum grid size in the peripheral non-core area is 2 m × 2 m. The multilayer damping boundary of 20 m is established at the left and right sides and the bottom of the model. In the model, the elastic subgrade thickness is 0.3 m. From top to bottom in order, the saturated foundation consists of a 0.3 m-thick upper permeable layer, 20 m-thick saturated soft soil layer, 9.3 m-thick lower permeable layer, and damping layer. The water table line is located at the bottom of the upper permeable layer, 0.6 m from the top of the subgrade.

In our simulations, the track is simplified as an Euler beam; the elastic subgrade, permeable layer, saturated soil layer, and damping layer in the model are simulated by using 2.5D saturated linear elastic units with 6 degrees of freedom. The material parameters of each layer are listed in Table 2, where the values of the saturated soil soft layer are taken with reference to the test results of the saturated soft clay soil in Xiaoshan, Hangzhou[46]. The material parameters of the horizontal damping layer are the same as those of the soil layer where they are located, and the material parameters of the vertical damping layer are the same as those of the permeable layer. The vehicle model is simulated using CRH2 body parameters (Table 3). The track material parameters are listed in Table 4.

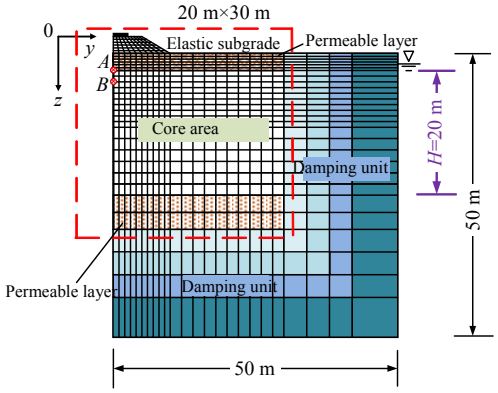

Fig. 3 Schematic view of half of the finite element model of the track–subgrade–saturated ground

3.1.2 Calculation conditions

The shear wave velocity of the saturated soil layer in the model is 83 m/s, and the Rayleigh wave velocity is 80 m/s. The train speeds calculated in this section for the numerical analysis are 3, 10, 30, 60, 64, 75, 80, 83, and 100 m/s. The Darcy permeability coefficients (k_D) considered for saturated soils are in seven groups from high to low: 10^{-3}, 10^{-4}, 10^{-5}, 10^{-6}, 10^{-7}, 10^{-8}, and 10^{-9} m/s. Two observation points are set along the axis of the model, namely A (0.7 m from the top surface of the subgrade and 0.1 m below the water table line) and B (1.2 m from the top surface of the subgrade and 0.6 m below the water table line).

3.2 Response analysis of excess pore pressure

3.2.1 Time-history curve of excess pore pressure

Figure 4 shows the evolution of the time-history curve of excess pore pressure at point *A* in saturated soft soil foundation with different train speeds and permeability coefficients.

Table 2 Parameters used for subgrade and foundation

Soil layer	Biot constant α	Biot constant M /MPa	Elastic modulus E /MPa	Shear modulus G /MPa	Poisson's ratio v	Soil grain density ρ_s /(kg • m^{-3})	Liquid density ρ_f /(kg • m^{-3})	Soil damping D_0	Porosity n	Permeability coefficient k_D /(m • s^{-1})
Subgrade	0.001	0.000 1	390.0	156.00	0.25	2 500	0.001	0.05	0.001	1×10^{-20}
Saturated soil	1.000	3 370.000 0	33.5	11.23	0.49	2 734	1 000.000	0.05	0.635	$1\times10^{-3}\sim1^{-9}$
Permeable layer	1.000	3 370.000 0	33.5	11.23	0.49	2 734	1 000.000	0.05	0.635	1

Table 3 Parameters used for CRH2 train

Carriage mass /kg	Bogie mass /kg	Wheelset mass /kg	Carriage length L /m	Center distance between adjacent bogies b /m	Bogie length a /m
45 000	3 600	1 700	24.8	14.9	2.5

Table 4 Parameters used to model the track (for two rails)

Mass per unit length of the rail m_r /(kg • m^{-1})	Rail bending stiffnessEI_r /(MN • m^2)	Mass per unit length of sleeper m_s /(kg • m^{-1})	Fastener stiffness k_p /(MN • m^{-1} • m^{-1})	Fastener dampingc_p /(kN • s • m^{-1} • m^{-1})	Contact area between track and foundation B /m^2
120	13.24	490	270	83.5	2.4

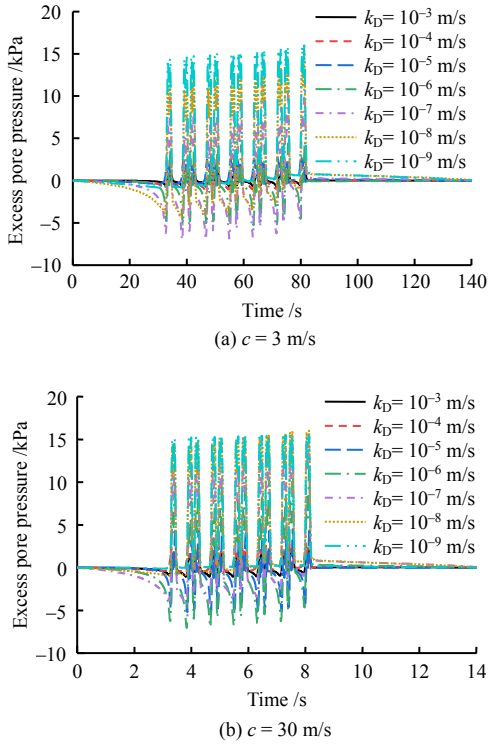

(a) c = 3 m/s

(b) c = 30 m/s

Fig. 4 Evolution of time-history curve of excess pore pressure

From Fig. 4(a), it can be seen that the response amplitude of the excess pore pressure increases as the soil permeability coefficient decreases at the same vehicle speed. The time-history curve amplitude of the excess pore pressure at point A is very small when the soil permeability coefficient is 10^{-3} m/s and 10^{-4} m/s, which is due to the large permeability coefficient of the soil, and the excess pore pressure caused by the train load is rapidly dissipated before it can be accumulated. As the permeability coefficient decreases, the dissipation rate of the excess pore pressure gets smaller gradually, thus increasing the amplitude of the excess pore pressure. Compared with Figs. 4(a) and 4(b), it can be observed that the higher the train speed, the larger the amplitude of excess pore pressure corresponding to the same permeability coefficient. This is because the higher the train speed, the shorter the interval between adjacent loads, and the excess pore pressure does not have enough time to dissipate, leading to the larger amplitude of excess pore pressure response in the end.

Figure 5 shows the maximum vertical displacement development at observation point A versus the train speed.

It can be seen from Fig. 5 that the soil permeability coefficient has almost no effect on the displacement response, and the amplitude of the displacement response is mainly controlled by the speed. For track-saturated soft soil foundation, there exists a critical velocity. When the train speed is lower than the critical velocity, the displacement response amplitude increases with the increase of the train speed. Otherwise, the displacement response amplitude decreases against the increase of the train speed. From Fig. 5, the critical velocity of the model could be determined as 80 m/s, consistent with the Rayleigh wave velocity of the saturated soil layer.

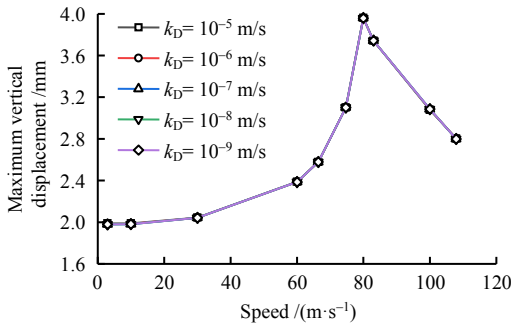

Fig. 5 Development of the maximum vertical displacement at point A versus train speed

Figure 6 shows the time-history curves of the excess pore pressure at observation point A when the permeability coefficient of the soil is 10^{-5} m/s and the train speed is below, equal to, and above the critical velocity of the system, respectively.

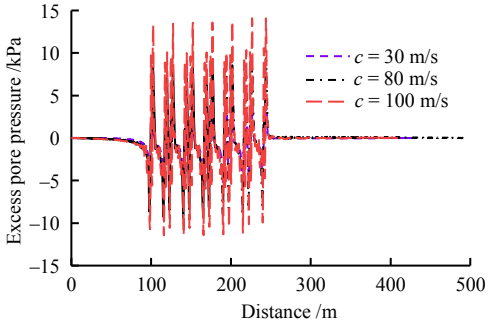

Fig. 6 Evolution of excess pore pressure at point A under different train speeds when soil permeability at 10^{-5} m/s

As can be seen in Fig. 6, regardless of the train speed, observation point A has a significant excess pore pressure response when the load is applied, and its response amplitude gradually increases with speed.

3.2.2 Variation of excess pore pressure along with the depth

Figure 7 shows the distribution of the maximum excess pore pressure along with the depth of the soil at different permeability coefficients for a train speed of 30 m/s.

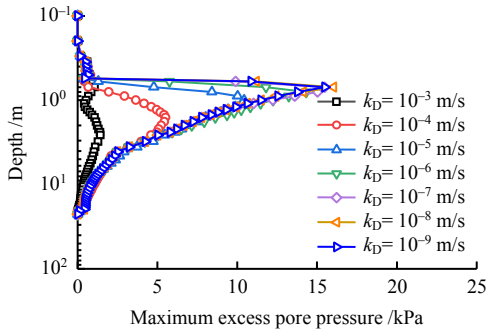

Fig. 7 Maximum excess pore pressures versus depth at different soil permeabilities

As shown in Fig. 7, there is almost no excess pore pressure in the depth range of elastic subgrade and upper permeable layer. In the saturated soil layer, the amplitude of excess pore pressure first increases with increasing depth and then decreases. This is because the shallow area near the upper permeable layer is easier to dissipate the excess pore pressure caused by the train load due to the short drainage distance. As the drainage distance increases with the depth, the excess pore pressure is more difficult to dissipate, so the excess pore pressure response amplitude gradually increases. However, with the further increase of depth, the load transferred to the soil gradually decreases due to the stress diffusion effect, resulting in the gradual decrease of the super-static pore pressure amplitude with depth. Further analysis reveals that the depth corresponding to the maximum excess pore pressure increases with the increase of permeability coefficient. When the permeability coefficient is 10^{-8} m/s, the depth corresponding to the maximum value is 0.7 m; when the permeability coefficient is 10^{-6} m/s, the corresponding depth is 0.8 m; when the permeability coefficient is 10^{-4} m/s, the corresponding depth is 1.6 m. The maximum excess pore pressure increases when the permeability coefficient declines for the same depth. The excess pore pressure at any permeability coefficient dissipates to lower than 0.8 kPa at a depth of 10 m.

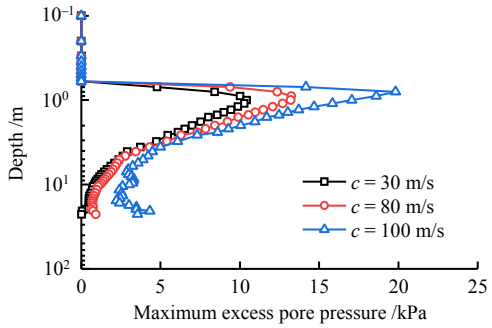

Fig. 8 Maximum excess pore pressures versus depth for different train speeds at the soil permeability of 10^{-5} m/s

Figure 8 shows the distribution of the maximum excess pore pressure along with the depth when the soil permeability coefficient is 10^{-5} m/s, and the train passes directly above the observation point at speeds below, equal to, and above the critical velocity, respectively.

As shown in Fig. 8, when the soil permeability coefficient is 10^{-5} m/s, the depth corresponding to the maximum excess pore pressure in the foundation decreases when train speed rises. When the train speed is 30 m/s, the depth corresponding to the maximum value is 1.6 m; when the train speed is 80 m/s, the depth corresponding to the maximum value is 0.9 m; when the train speed is 100 m/s, the depth corresponding to the maximum value is 0.8 m. The maximum excess pore pressure increases with train speed for the same depth. When the train speed does not exceed the critical velocity, the excess pore pressure dissipates to below 0.8 kPa at a depth of 10 m. Otherwise, there is still a significant excess pore pressure response below a depth of 10 m.

3.2.3 Effect of c/k_D on excess pore pressure

The evolution of excess pore pressure with time indicates that the larger the permeability coefficient, the smaller the excess pore pressure response for the same train speed; the larger the train speed, the larger the excess pore pressure response for the same permeability coefficient. To this end, the ratio of train speed to soil permeability coefficient is defined as c/k_D t investigate the variations of the excess pore pressure.

Figure 9 shows the variations of the maximum excess pore pressure when values of c/k_D change at observation point *A* and *B*.

It could be observed from Fig. 9(a) that the maximum excess pore pressure at point *A* is independent of the train speed and controlled only by c/k_D when the train speed is lower than the critical velocity. When c/k_D <3×104, the maximum excess pore pressure is close to 0; when 3×104≤ c/k_D ≤ 109, the excess pore pressure increases gradually with the c/k_D value; when c/k_D >109, the maximum excess pore pressure remains unchanged. This phenomenon indicates that the variations of excess pore pressure based on the parameters c/k_D are monotonic, and there is a critical c/k_D value, which is 10^9 for point *A*. When the train speed exceeds the critical velocity, the trend of the maximum excess pore pressure variations with c/k_D is similar to the cases at other speeds. Still, the corresponding maximum excess pore pressure is larger than that of the other speeds, indicating that the maximum excess pore pressure at a speed higher than the critical velocity is determined by both the parameter c/k_D and the train speed.

Figure 9(b) shows that the variation curve of the maximum excess pore pressure at observation point *B* is similar to that at point *A*. When c/k_D <×10^4, the

maximum excess pore pressure is close to 0; when $3\times10^4 \leqslant c/k_D \leqslant 3\times10^7$, the excess pore pressure increases gradually with the c/k_D value; when $c/k_D > 3\times10^7$, the maximum excess pore pressure remains unchanged. When the train speed exceeds the critical velocity, the trend of the maximum excess pore pressure variations with c/k_D is similar to the cases at other speeds. However, the corresponding maximum excess pore pressure is larger than that of the other speeds. For point *B*, the critical c/k_D value is 3×10^7. Compared with Figs. 9(a) and 9(b), it can be concluded that the critical c/k_D value decreases when depth increases.

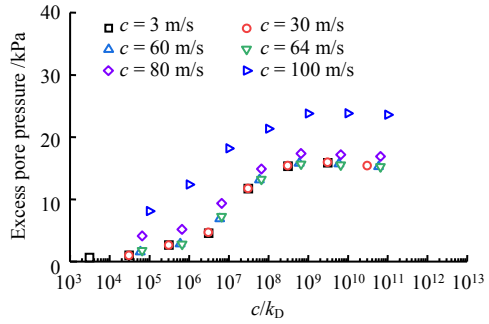

(a) Point *A* (z = 0.7 m)

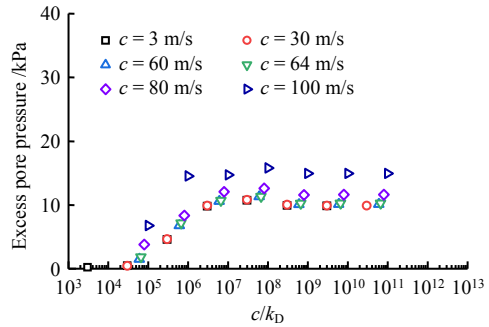

(b) Point *B*(z = 1.2 m)

Fig. 9 Dependence of maximum excess pore pressure on c/k_D

3.2.4 Contours of excess pore pressure

Figure 10 shows the excess pore pressure distribution in the *YZ* plane when the train is applied directly above the observation section.

Figures 10(a), 10(c), and 10(e) correspond with c/k_D values are 3×10^4, 8×10^4, and 10^5, respectively. The distribution contours show that only the excess pore pressure response is negligible in the whole *YZ* plane. When the c/k_D value reaches or exceeds 3×10^9 (Figs. 10(b), 10(d), and 10(f)), a significant excess pore pressure response appears inside the saturated foundation with a parabolic distribution in the *YZ* plane. In terms of the distribution range, it can be found that the distribution width and depth of the excess pore pressure increase with c/k_D values, especially in the area where excess pore pressure is above 10 kPa.

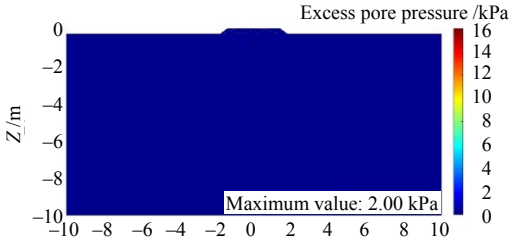

(a) c = 30 m/s，$k_D = 10^{-3}$ m/s（$c/k_D = 3\times10^4$）

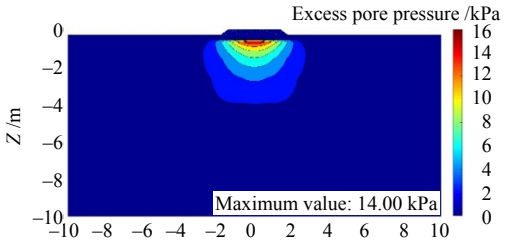

(b) c = 30 m/s，$k_D = 10^{-8}$ m/s（$c/k_D = 3\times10^9$）

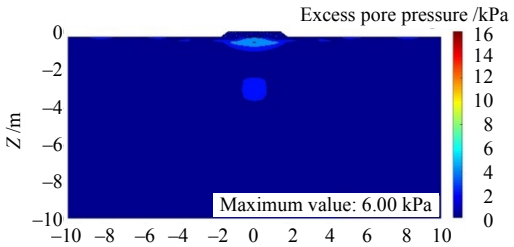

(c) c = 80 m/s，$k_D = 10^{-3}$ m/s（$c/k_D = 8\times10^4$）

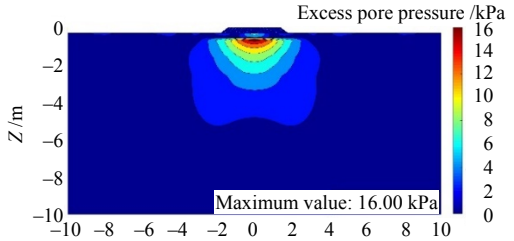

(d) c = 80 m/s，$k_D = 10^{-8}$ m/s（$c/k_D = 8\times10^9$）

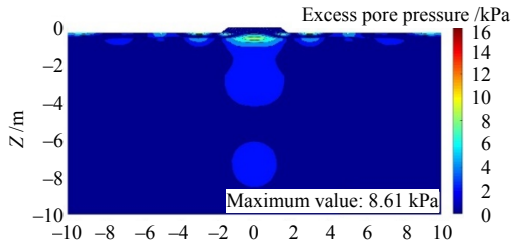

(e) c = 100 m/s，$k_D = 10^{-3}$ m/s（$c/k_D = 10^5$）

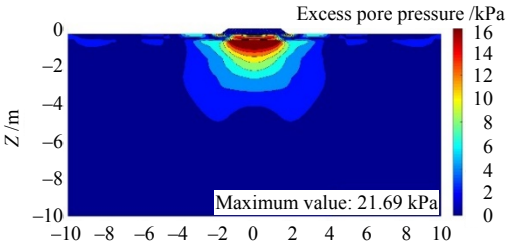

(f) c = 100 m/s，$k_D = 10^{-8}$ m/s（$c/k_D = 10^{10}$）

Fig. 10 Excess pore pressure contours under different train speeds and soil permeabilities in *YZ* plane

3.3 Effective stress response analysis

3.3.1 Effect of the ratio of train speed to soil permeability coefficient (c / k_{D}) on effective stress

Figure 11 shows the maximum effective stress at observation points *A* and *B* as a function of c / k_{D} .

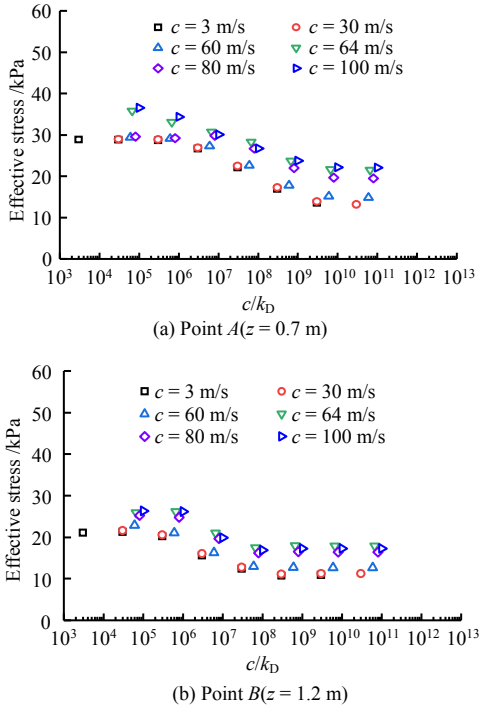

Fig. 11 Dependence of the maximum effective stress on c/k_{D}

From Fig. 11(a), it can be seen that the maximum effective stress at point *A* is independent of the load speed and only influenced by c / k_{D} when the train speed is low (≤30 m/s). When c / k_{D} is less than 3×10^4, the maximum effective stress is close to 30 kPa; when it is greater than 3×10^4 and less than the critical value, the effective stress gradually decreases as c / k_{D} increases; when it is higher than the critical value, the maximum effective stress almost remains constant. With the increase of the train speed, the maximum effective stress changing with c / k_{D} is similar to that at the low speed, but the maximum effective stress corresponding with the same c / k_{D} increases significantly. The maximum effective stress variation trend at observation point *B* is similar to that at point *A*. At low velocity, the maximum effective stress is close to 20 kPa when c / k_{D} is less than 3×10^4 and then decreases gradually as c / k_{D} rises, finally remaining unchanged after c / k_{D} reaching the critical value. Comparing Figs. 11(a) and 11(b), it can be concluded that the critical value of c / k_{D} corresponding with effective stress and the critical value of c / k_{D} in excess pore pressure is consistent. And the critical c / k_{D} value decreases with increasing depth. However, the effective stress is more sensitive to the change in velocity compared with the excess pore pressure.

3.2.3 Contours of effective stress

Figure 12 shows the effective stress distribution in the *YZ* plane when the train load is directly above the observed section.

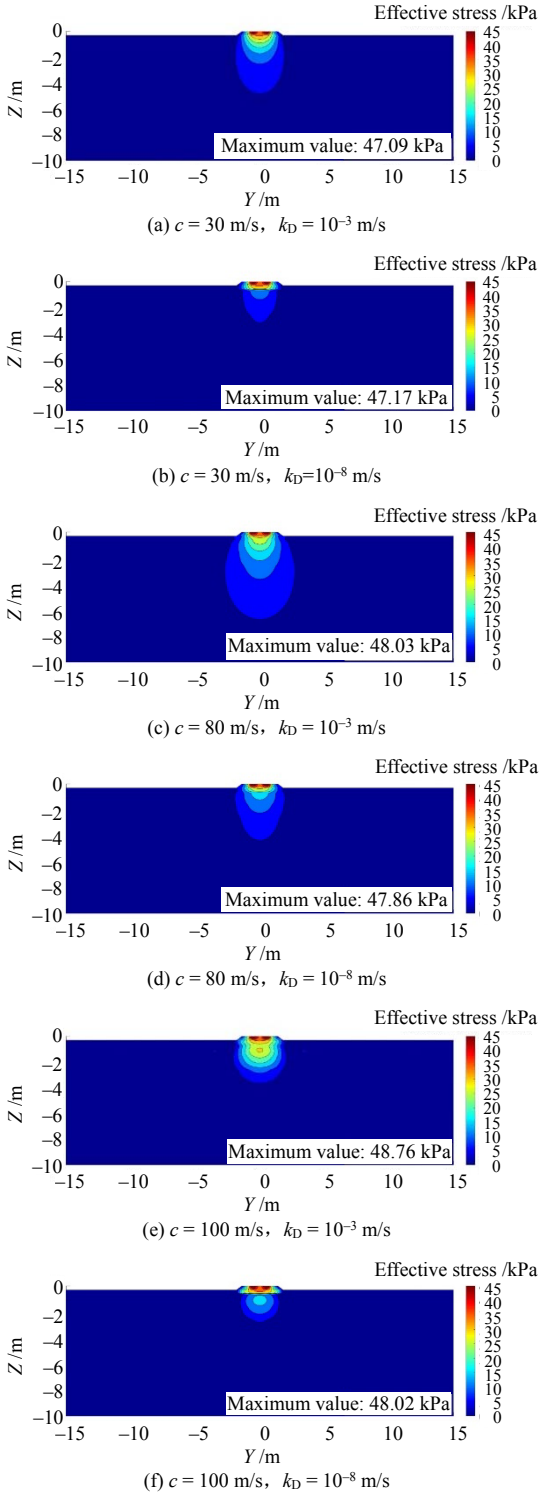

Fig. 12 Effective stress contours under different train speeds and soil permeabilities in *YZ* plane

As shown in Fig. 12, when the soil permeability coefficient is 10^{-3} m/s, and the train load is directly applied above the observed section, the effective stress response inside the foundation is mainly concentrated

at the position of the train axle and distributed in a smooth parabolic pattern in the *YZ* plane. The maximum effective stress increases slowly with the vehicle speed, and the effect depth by the stress higher than 10 kPa gradually increases from 2 m to 5 m below the subgrade surface. When the permeability coefficient is below 10^{-8} m/s, the high stress area is mainly distributed in the subgrade and permeable layer, and the effective stress inside the saturated foundation is small and decays to below 5 kPa about 5 m below the top surface of the subgrade. Thus, it can be concluded that the effective stress response inside the foundation is influenced by the permeability coefficient of the soil and the train speed. At the same speed, the influencing zone of the effective stress decreases when the permeability coefficient decreases, and the zone is greatest when the train speed reaches the critical velocity.

3.4 Displacement response analysis

3.4.1 Analysis of displacement variation with c / k_D

Figure 13 shows the dependence of the maximum vertical displacement on c / k_D at observation points *A* and *B* under the train loads.

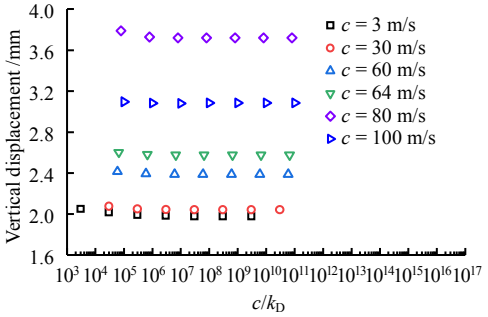

(a) Point *A*, *z* = 0.7 m

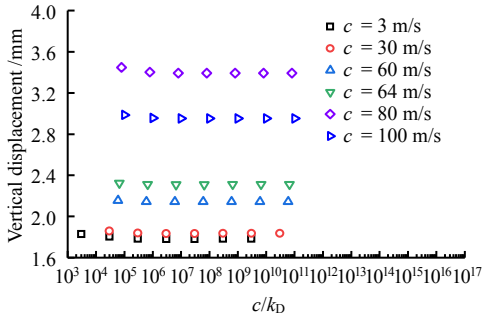

(b) Point *B*, *z* = 1.2 m

Fig. 13 Dependence of displacement on c/k_D

From Fig. 13(a), the displacement response at point *A* is independent of c / k_D. When the train speed is greater than 60 m/s, the response of vertical displacement increases significantly with speed. The trend of vertical displacement at point *B* in Fig. 13(b) is consistent with that at point A. Compared with the two figures in Figs. 13(a) and 13(b), it is found that the maximum vertical displacement decreases as the depth increase at the same train speed.

3.4.2 Mach effect

Figure 14 shows the displacement distribution in the *XY* plane (*z*=0.3 m from foundation surface) when a certain train axle is directly above the observation section.

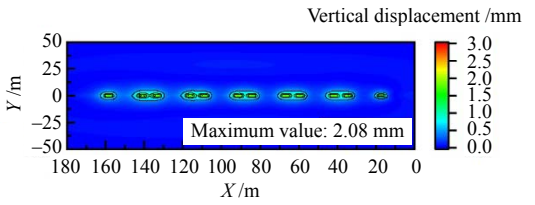

(a) c = 30 m/s, $k_D = 10^{-3}$ m/s

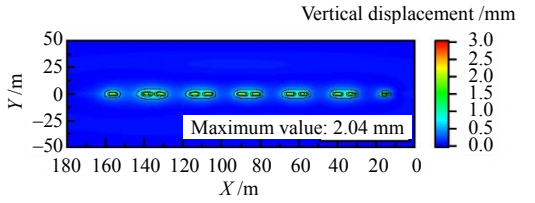

(b) c = 30 m/s, $k_D = 10^{-8}$ m/s

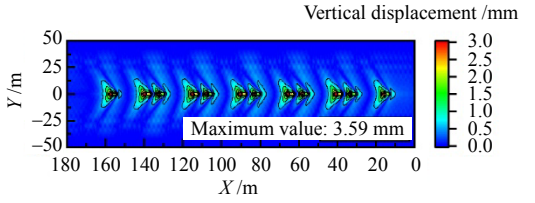

(c) c = 80 m/s, $k_D = 10^{-3}$ m/s

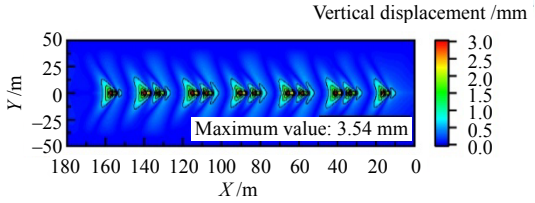

(d) c = 80 m/s, $k_D = 10^{-8}$ m/s

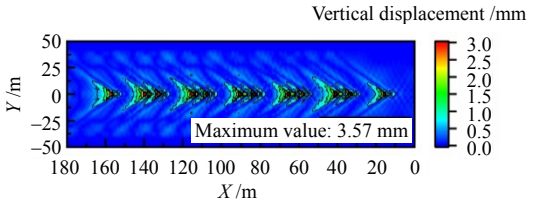

(e) c = 100 m/s, $k_D = 10^{-3}$ m/s

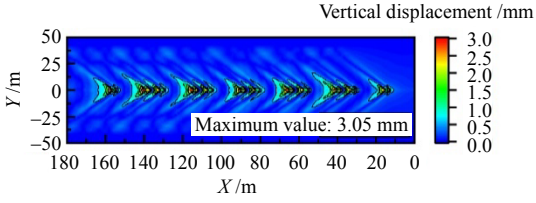

(f) c = 100 m/s, $k_D = 10^{-8}$ m/s

Fig. 14 Mach effect under train load with different speeds and soil permeabilities

The permeability coefficient of the saturated soil in Fig. 14(a) is 10^{-3} m/s, and the train speed is 30 m/s. In this case, the displacement response of the foundation is distributed in a circular shape, and the distribution

range is concentrated at the position of the axle. There is almost no wave propagation in the foundation, and the maximum displacement response is 2.08 mm. When the permeability coefficient is reduced to 10^{-8} m/s (Fig. 14(b)), the displacement response distribution is similar to Fig. 14(a), and the maximum displacement response is 2.04 mm.

Figure 14(c) corresponds to a train speed of 80 m/s and a permeability coefficient of 10^{-3} m/s, and Fig. 14(d) corresponds to a train speed of 80 m/s and a permeability coefficient of 10^{-8} m/s. The train speed reaches the critical velocity, and the deformation in the foundation is significant. There are small-scale regional vibrations in both the front and rear areas of the axle position, and deformation of the surface is in the form of a fluctuating line extending backward from the location of the train load. Obvious two narrow wings in the distribution of the displacement response appear behind the train load, forming Mach cone, and the displacement response shows the Mach effect phenomenon. Figures 14(e) and 14(f) correspond to the train speed of 100 m/s with a permeability coefficient of 10^{-3} m/s and the train speed of 100 m/s with a permeability coefficient of 10^{-8} m/s, respectively, where the train speed exceeds the critical velocity and the Mach effect is further enhanced, leading to a more narrow Mach cone with smaller angle and wider propagation area of vibration. It can be concluded that when the train speed is no less than the critical velocity, there will be significant wave propagation in the saturated foundation, and the Mach effect of displacement response will also be notable, and the Mach effect will be strengthened with the increase of train speed.

4 Conclusions

(1) When the train speed is less than the critical velocity, the maximum excess pore pressure caused by the train load in the saturated soil is determined by the ratio of the train speed to the soil permeability coefficient (c / k_{D}), which exists a critical value. When c / k_{D} is lower than the critical value, the excess pore pressure increases with c / k_{D} ; otherwise, the excess pore pressure remains constant. The critical c / k_{D} depends on the depth, and increasing depth reduces the critical c / k_{D} value.

(2) When the train speed is no less than the critical velocity, the variation trend of excess pore pressure with c / k_{D} is similar to that at low speed, but the maximum excess pore pressure corresponding to the same c / k_{D} value is larger than that at low speed, indicating that the maximum excess pore pressure is determined by both the parameter c / k_{D} and the train speed.

(3) In terms of the effective stress response, there also exists a critical c / k_{D} value, and the value is the same as the critical value in the excess pore pressure response. When the train speed is low, the maximum effective stress is independent of the train speed and is only controlled by c / k_{D} .

(4) The displacement response is mainly influenced by the train speed and is almost independent of the soil permeability coefficient. Similar to elastic foundations, a significant Mach effect occurs inside saturated foundations when the train speed reaches or exceeds the critical velocity.

(5) For the typical saturated soft clay with low permeability in the southeast coast, even when the train runs at a low speed (108 km/h), the excess pore pressure in the saturated foundation will be nearly 10 kPa, and the single-phase elastic foundation model is no longer applicable. And when the train passes at high speed (360 km/h), the maximum excess pore pressure in the saturated soft ground can reach about 23 kPa.

References

[1] BIOT M A. Theory of propagation of elastic waves in a fluid-saturated porous solid. I. Low frequency range[J]. The Journal of the Acoustical Society of America, 1956, 28(2): 179–191.

[2] BIOT M A. Theory of propagation of elastic waves in a fluid-saturated porous solid. II. Higher frequency range[J]. The Journal of the Acoustical Society of America, 1956, 28(2): 179–191.

[3] ZIENKIEWICZ O C, SHIOMI T. Dynamic behaviour of saturated porous media: the generalized Biot formulation and its numerical solution[J]. International Journal for Numerical and Analytical Methods in Geomechanics, 1984, 8(1): 71–96.

[4] SIDDHARTHAN R, ZAFIR Z, NORRIS G M. Moving load response of layered soil. I: formulation[J]. Journal of Engineering Mechanics, 1993, 119(10).

[5] LU J F, HANYGA A. Fundamental solution for a layered porous half space subject to a vertical point force or a point fluid source[J]. Computational Mechanics, 2004, 35(5): 376–391.

[6] LU J F, JENG D S. A half-space saturated poro-elastic medium subjected to a moving point load[J]. International Journal of Solids and Structures, 2007, 44(2): 573–586.

[7] GAO G Y, CHEN Q S, HE J F, LIU F. Investigation of ground vibration due to trains moving on saturated multi-layered ground by 2.5 D finite element method[J].

Soil Dynamics and Earthquake Engineering, 2012, 40: 87–98.

[8] HE C, ZHOU S, DI H, et al. A 2.5-d coupled Fe-Be model for the dynamic interaction between tunnel and saturated soil[J]. Chinese Journal of Theoretical and Applied Mechanics, 2017, 49(1): 126–136.

[9] HE C, ZHOU S, GUO P, et al. Dynamic 2.5-D green's function for a point load or a point fluid source in a layered poroelastic half-space[J]. Engineering Analysis with Boundary Elements, 2017(77): 123–137.

[10] YUAN Zong-hao, CAI Yuan-qiang, ZENG Chen. Dynamic response of track system and underground railway tunnel in saturated soil subjected to moving train loads[J]. Chinese Journal of Rock Mechanics and Engineering, 2015, 34(7): 1470–1479.

[11] ZENG Chen, SUN Hong-lei, CAI Yuan-qiang. Analysis of three-dimensional dynamic response of a circular lining tunnel in saturated soil to harmonic loading[J]. Rock and Soil Mechanics, 2014, 35(4): 1147–1156.

[12] GAO Guang-yun, HE Jun-feng, LI Jia. Dynamic response induced by running subway in saturated ground[J]. Journal of Zhejiang University (Engineering Science), 2010, 44(10): 1925–1950.

[13] GAO Guang-yun, HE Jun-feng, YANG Chen-bin, et al. Ground vibration induced by trains moving on saturated ground using 2.5D FEM[J]. Chinese Journal of Geotechnical Engineering, 2011, 33(2): 234–241.

[14] YUAN Wan, CAI Yuan-qiang, SHI Li, et al. Study of vibration-isolation efficiency of open trench in saturated ground by 2.5D finite element method[J]. Rock and Soil Mechanics, 2013, 34(7): 2111–2118.

[15] JIN B. Dynamic responses of a poroelastic half space generatedby high speed load[J]. Chinese Quarterly of Mechanics, 2004(2): 168–174.

[16] CAI Y Q, SUN H, XU C. Response of railway track system on poroelastic half-space soil medium subjected to a moving train load[J]. International Journal of Solids and Structures, 2008, 45(18-19): 5015–5034.

[17] CAI Y Q, SUN H, XU C. Three-dimensional analyses of dynamic responses of track–ground system subjected to a moving train load[J]. Computers and Structures, 2008, 86(7–8): 816–824.

[18] THEODORAKOPOULOS D D. Dynamic analysis of a poroelastic half-plane soil medium under moving loads[J]. Soil Dynamics and Earthquake Engineering, 2003, 23(7): 521–533.

[19] THEODORAKOPOULOS D D, CHASSIAKOS A P, BESKOS D E. Dynamic effects of moving load on a poroelastic soil medium by an approximate method[J]. International Journal of Solids and Structures, 2004, 41(7): 1801–1822.

[20] LI Shao-yi, GAO Guang-yun, GU Xiao-qiang. Influence of pore water pressure on dynamic response of high-speed rail subgrade[J]. China Earthquake Engieering Journal, 2014, 36(4): 881–891.

[21] QIAN Jian-gu, ZHOU Ren-yi, HUANG Mao-song. Dynamic stress responses to high-speed moving load on elastic saturated semi-space ground[J]. Engineering Mechanics, 2016, 33(3): 47–54.

[22] YUAN Z H, CAI Y Q, CAO Z G. An analytical model for vibration prediction of a tunnel embedded in a saturated full-space to a harmonic point load[J]. Soil Dynamics and Earthquake Engineering, 2016, 86: 25–40.

[23] YUAN Z H, XU C, CAI Y Q, CAO Z G. Dynamic response of a tunnel buried in a saturated poroelastic soil layer to a moving point load[J]. Soil Dynamics and Earthquake Engineering, 2015, 77: 348–359.

[24] DI H, ZHOU S H, HE C, ZHANG X H, LUO Z. Three-dimensional multilayer cylindrical tunnel model for calculating train-induced dynamic stress in saturated soils[J]. Computers and Geotechnics, 2016, 80: 333–345.

[25] DI H, ZHOU S H, LUO Z, et al. A vehicle-track-tunnel-soil model for evaluating the dynamic response of a double-line metro tunnel in a poroelastic half-space[J]. Computers and Geotechnics, 2017, 101(9): 245–263.

[26] HE Chao, ZHOU Shun-hua, DI Hong-gui, XIAO Jun-hua. A 2.5-D coupled FE-BE model for the dynamic interaction between tunnel and saturated soil[J]. Chinese Journal of Theoretical and Applied Mechanics, 2017, 49(1): 126–136.

[27] CAI Yuan-qiang, ZHAO Guo-xing, ZHENG Zao-feng, et al. Vertical vibration analysis of transversely isotropic saturated soils with elastic superstratum[J]. Journal of Zhejing University (Engineering Science), 2006, 40(2): 267–271.

[28] GAO Guang-yun, CHENG Gong-qi, LI Jia. Numerical analysis of dynamic characteristic of transversely isotropic satureted soil foundation subjected to high-speed train load[J]. Chinese Journal of Rock Mechanics and Engineering, 2014, 33(1): 189–198.

[29] BA Z, KANG Z, LEE V W. Plane strain dynamic responses of a multi-layered transversely isotropic saturated half-space[J]. International Journal of Engineering Science, 2017, 119: 55–77.

[30] BA Z, WU M, LIANG J. 3D dynamic responses of a multi-layered transversely isotropic saturated half-space under concentrated forces and pore pressure[J]. Applied Mathematical Modelling, 2020, 80: 859–878.

[31] LI Yi-cheng, FENG Shi-jin. Dynamic response of a track coupled with a transversely isotropic ground duo to train loads[J]. Rock and Soil Mechanies, 2021, 42(5): 1313–1324.

[32] YANG Yi-min. Dynamic responses of stratified poroelastic soft soil foundation under high speed train load[D]. Hangzhou: Zhejiang University, 2017.

[33] AI Z Y, JI W T, LI Y, et al. Dynamic response of saturated multilayered soils with elastic superstrata subjected to vertical impulsive loadings[J]. Applied Mathematical Modelling, 2021, 91: 875–891.

[34] ZHAI W, HE Z, SONG X. Prediction of high-speed train induced ground vibration based on train-track-ground system model[J]. Earthquake Engineering and Engineering Vibration, 2010, 9(4): 545–554.

[35] KAYNIA A M. Ground vibration from high-speed trains: Prediction and countermeasure[J]. Journal of Geotechnical and Geoenvironmental Engineering, 2000, 126(6): 531–537.

[36] MADSHUS C, KAYNIA A M. Dynamic ground interaction: a critical issue for high speed train lines on soft soil[C]//Geotechnical Engineering for Transportation Infrastructure. [S. l.]: Theory and Practice, 1999.

[37] AUERSCH L. The effect of critically moving loads on the vibrations of soft soils and isolated railway tracks[J]. Journal of Sound and Vibration, 2008, 310: 587–607.

[38] BIAN X, CHENG C, JIANG J, et al. Numerical analysis of soil vibrations due to trains moving at critical speed[J]. Acta Geotechnica, 2016, 11(2): 281–294.

[39] COSTA P A, COLACO A C, CALCADA R, et al. Critical speed of railway tracks. Detailed and simplified approaches[J]. Transportation Geotechnics, 2015(2): 30–46.

[40] HU J, BIAN X, JIANG J. Critical velocity of high-speed train running on soft soil and induced dynamic soil response[J]. Procedia Engineering, 2016, 143: 1034–1042.

[41] HU J, BIAN X, XU W, et al. Investigation into the critical speed of ballastless track[J]. Transportation Geotechnics, 2018, 18: 142–148.

[42] BIOT M A. Mechanics of deformation and acoustic propagation in porous media[J]. Journal of Applied Physics, 1962, 33(4): 1482–1498.

[43] BIAN X, HU J, THOMPSON D, POWRIE W. Pore pressure generation in a poro-elastic soil under moving train loads[J]. Soil Dynamics and Earthquake Engineering, 2019, 125: 105711.

[44] TAKEMIYA H, BIAN X C. Substructure simulation of inhomogeneous track and layered ground dynamic interaction under train passage[J]. Journal of Engineering Mechanics, 2005, 131(7): 699–711.

[45] LIU G R, JERRY S. A non-reflecting boundary for analyzing wave propagation using the finite element method[J]. Finite Elements in Analysis and Design, 2003, 39: 403–417.

[46] XIE Kang-he, ZHUANG Ying-chun, LI Xi-bin. Laboratory investigation of permeability characteristics of Xiaoshan clay[J]. Chinese Journal of Geotechnical Engineering, 2005, 27(5): 591–594.

Appendix A

$$\boldsymbol{K}_1 = \sum_e \int_{-1}^{1}\int_{-1}^{1} (\boldsymbol{B} * \boldsymbol{N})^{\mathrm{T}} \boldsymbol{D}\boldsymbol{B}\boldsymbol{N} \left|\boldsymbol{J}\right| \mathrm{d}\eta \mathrm{d}\zeta \tag{A1}$$

$$\boldsymbol{K}_2 = (\alpha^2 M) \sum_e \int_{-1}^{1}\int_{-1}^{1} (\boldsymbol{B} * \boldsymbol{N})^{\mathrm{T}} \boldsymbol{m}\boldsymbol{m}^{\mathrm{T}} \boldsymbol{B}\boldsymbol{N} \left|\boldsymbol{J}\right| \mathrm{d}\eta \mathrm{d}\zeta \tag{A2}$$

$$\boldsymbol{K}_3 = (\alpha M) \sum_e \int_{-1}^{1}\int_{-1}^{1} (\boldsymbol{B} * \boldsymbol{N})^{\mathrm{T}} \boldsymbol{m}\boldsymbol{m}^{\mathrm{T}} \boldsymbol{B}\boldsymbol{N} \left|\boldsymbol{J}\right| \mathrm{d}\eta \mathrm{d}\zeta \tag{A3}$$

$$\boldsymbol{M}_1 = \omega^2 \rho_b \sum_e \int_{-1}^{1}\int_{-1}^{1} \boldsymbol{N}^{\mathrm{T}} \boldsymbol{N} \left|\boldsymbol{J}\right| \mathrm{d}\eta \mathrm{d}\zeta \tag{A4}$$

$$\boldsymbol{M}_2 = \boldsymbol{M}_3 = \omega^2 \rho_f \sum_e \int_{-1}^{1}\int_{-1}^{1} \boldsymbol{N}^{\mathrm{T}} \boldsymbol{N} \left|\boldsymbol{J}\right| \mathrm{d}\eta \mathrm{d}\zeta \tag{A5}$$

$$\boldsymbol{M}_4 = (\omega^2 m - i\omega \frac{\rho_f g}{k_D}) \sum_e \int_{-1}^{1}\int_{-1}^{1} \boldsymbol{N}^{\mathrm{T}} \boldsymbol{N} \left|\boldsymbol{J}\right| \mathrm{d}\eta \mathrm{d}\zeta \tag{A6}$$

$$\boldsymbol{L}_1 = \alpha M \sum_e \int_{-1}^{1}\int_{-1}^{1} (\boldsymbol{B} * \boldsymbol{N})^{\mathrm{T}} \boldsymbol{m}\boldsymbol{m}^{\mathrm{T}} \boldsymbol{B}\boldsymbol{N} \left|\boldsymbol{J}\right| \mathrm{d}\eta \mathrm{d}\zeta \tag{A7}$$

$$\boldsymbol{L}_2 = M \sum_e \int_{-1}^{1}\int_{-1}^{1} (\boldsymbol{B} * \boldsymbol{N})^{\mathrm{T}} \boldsymbol{m}\boldsymbol{m}^{\mathrm{T}} \boldsymbol{B}\boldsymbol{N} \left|\boldsymbol{J}\right| \mathrm{d}\eta \mathrm{d}\zeta \tag{A8}$$

$$\tilde{\tilde{\boldsymbol{F}}}^{\mathrm{s}} = \sum_e \int_{-1}^{1} \boldsymbol{N}^{\mathrm{T}} \tilde{\tilde{f}} \left|\boldsymbol{J}\right| \mathrm{d}\eta \tag{A9}$$

$$\tilde{\tilde{\boldsymbol{F}}}^{\mathrm{f}} = \sum_e \int_{-1}^{1} \boldsymbol{N}^{\mathrm{T}} \tilde{\tilde{q}} \left|\boldsymbol{J}\right| \mathrm{d}\eta \tag{A10}$$

$$\boldsymbol{D}=\begin{bmatrix}\lambda+2\mu & \lambda & \lambda & 0 & 0 & 0\\ \lambda & \lambda+2\mu & \lambda & 0 & 0 & 0\\ \lambda & \lambda & \lambda+2\mu & 0 & 0 & 0\\ 0 & 0 & 0 & \mu & 0 & 0\\ 0 & 0 & 0 & 0 & \mu & 0\\ 0 & 0 & 0 & 0 & 0 & \mu\end{bmatrix} \quad (A11)$$

$$\boldsymbol{B}=\begin{bmatrix}-i\xi_x & 0 & 0\\ 0 & \dfrac{\partial}{\partial_y} & 0\\ 0 & 0 & \dfrac{\partial}{\partial_z}\\ \dfrac{\partial}{\partial_y} & -i\xi_x & 0\\ 0 & \dfrac{\partial}{\partial_z} & \dfrac{\partial}{\partial_y}\\ \dfrac{\partial}{\partial_z} & 0 & -i\xi_x\end{bmatrix} \quad (A12)$$

$$\boldsymbol{m}=\begin{bmatrix}1\\1\\1\\0\\0\\0\end{bmatrix} \quad (A13)$$

$$|\boldsymbol{J}|=\begin{vmatrix}\sum_{i=1}^{4}\dfrac{\partial N_i}{\partial\eta}y_i^e & \sum_{i=1}^{4}\dfrac{\partial N_i}{\partial\xi}y_i^e\\ \sum_{i=1}^{4}\dfrac{\partial N_i}{\partial\eta}z_i^e & \sum_{i=1}^{4}\dfrac{\partial N_i}{\partial\xi}z_i^e\end{vmatrix} \quad (A14)$$

where $\boldsymbol{e}$ represents element; $\boldsymbol{N}$ represents shape function; $|\boldsymbol{J}|$ is the determinant of Jacobi matrix; η and ζ are variables of local coordinate; $\boldsymbol{f}$ is an external force acting on the element; and q is flux at element.